



Article

Fabrication of Cu₂O/CuO Nanowires by One-Step Thermal Oxidation of Flexible Copper Mesh for Supercapacitor Applications

Mina-Ionela Morariu (Popescu)^{1,2,†}, Mircea Nicolaescu^{1,†}, Iosif Hulka³ , Narcis Duțeanu² , Corina Orha¹, Carmen Lăzău^{1,*} and Cornelia Bandas^{1,*}

¹ Condensed Matter Department, National Institute for Research and Development in Electrochemistry and Condensed Matter Timisoara, 300224 Timisoara, Romania; mina.popescu@student.upt.ro (M.-I.M.); nicolaescu.mircea13@yahoo.com (M.N.); orha.corina@gmail.com (C.O.)

² Department of Applied Chemistry and Engineering of Inorganic Compounds and Environment, Politehnica University of Timisoara, 300223 Timisoara, Romania; narcis.duteanu@upt.ro

³ Research Institute for Renewable Energies, Politehnica University of Timisoara, 300501 Timisoara, Romania; iosif.hulka@upt.ro

* Correspondence: carmen.lazau@gmail.com (C.L.); cornelia.bandas@gmail.com (C.B.)

† These authors contributed equally to this work.

Abstract: This study focuses on the growth of Cu₂O/CuO nanowires by one-step thermal oxidation using a flexible copper mesh at oxidation temperatures in the range of 300 to 600 °C in a controlled atmosphere of mixed-flow Ar and O₂ gases. Thermal oxidation is one of the simplest used methods to obtain nanowires on a metal surface, offering advantages such as low production costs and the ability to produce metal oxides on a large scale without the use of hazardous chemical compounds. The growth of metal oxides on a conductive substrate, forming metal/oxide structures, has proven to be an effective method for enhancing charge-transfer efficiency. The as-synthesized Cu/Cu₂O/CuO (Nw) electrodes were structurally and morphologically characterized using techniques such as XRD and SEM/EDX analysis to investigate the structure modification and morphologies of the materials. The supercapacitor properties of the as-developed Cu/Cu₂O/CuO (Nw) electrodes were then examined using cyclic voltammetry (CV), galvanostatic charge–discharge (GCD) measurements, and electrochemical impedance spectroscopy (EIS). The CV curves show that the Cu/Cu₂O/CuO (Nw) structure acts as a positive electrode, and, at a scan rate of 5 mV s⁻¹, the highest capacitance values reached 26.158 mF cm⁻² for the electrode oxidized at a temperature of 300 °C. The assessment of the flexibility of the electrodes was performed at various bending angles, including 0°, 45°, 90°, 135°, and 180°. The GCD analysis revealed a maximum specific capacitance of 21.198 mF cm⁻² at a low power density of 0.5 mA cm⁻² for the oxidation temperature of 300 °C. The cycle life assessment of all of the as-obtained Cu/Cu₂O/CuO (Nw) electrodes over 500 cycles was performed by GCD analysis, which confirmed their electrochemical stability.



Citation: Morariu, M.-I.; Nicolaescu, M.; Hulka, I.; Duțeanu, N.; Orha, C.; Lăzău, C.; Bandas, C. Fabrication of Cu₂O/CuO Nanowires by One-Step Thermal Oxidation of Flexible Copper Mesh for Supercapacitor Applications. *Batteries* **2024**, *10*, 246. <https://doi.org/10.3390/batteries10070246>

Academic Editor: Douglas Ivey

Received: 4 June 2024

Revised: 3 July 2024

Accepted: 7 July 2024

Published: 10 July 2024



Copyright: © 2024 by the authors. Licensee MDPI, Basel, Switzerland. This article is an open access article distributed under the terms and conditions of the Creative Commons Attribution (CC BY) license (<https://creativecommons.org/licenses/by/4.0/>).

1. Introduction

Recently, electronic devices, especially supercapacitors, have gained great attention as energy storage devices due to their high power density, fast charge/discharge rates, stability, wide operating temperature range, long cycle life, relatively simple structures, and low cost [1]. Depending on the reaction mechanisms involved, supercapacitors can be classified into electrical pseudo-capacitors and double-layer capacitors (EDLCs) [2]. Pseudo-capacitors, in particular, offer considerably better energy density and specific capacitance compared to those of EDLCs because they store energy within the electrode via the

faradic redox reaction using conducting polymers and metal oxides as electrode materials. However, many poorly understood issues draw many researchers who dedicate their time to solve them, and the assignment of some additional characteristics such as environmental friendliness, wearability, and energy-level indicators in supercapacitors brings them closer to realistic applications [3]. In order to achieve excellent capacitive performance for pseudo-supercapacitors, most of the research studies have focused on the development of high-performance materials, considering various metal substrates such as stainless steel [4], nickel [5], titanium [6], and copper [7,8]; and transition metal oxides/hydroxides, such as RuO₂ [9], NiO [10], Ni(OH)₂ [11,12], Ni_{0.5}Mn_{0.5}Co₂O₄@Co₃O₄ [13], MnO₂ [14], Co₃O₄ [15], Co(OH)₂ [16], V₂O₅ [17], CuO [18–20], Cu₂O [21,22], and CO₃O₄ [23] as electrode materials. Over time, some researchers have focused on the development of hybrid structures used for supercapacitor application, one of these being successfully obtained by our team, such as the Zn-ZnO(Nw)-rGO hybrid electrode synthesized by the one-step microwave-assisted hydrothermal method [24]. The electrochemical measurements demonstrate the behavior as a negative electrode exhibiting a rectangular, non-ideal shape, suggesting that the electrode behaves as a pseudo-capacitor [24]. Another interesting material is represented by flexible materials, which open a new trend due to their potential applications in a variety of fields, including wearable technology, portable electronics, and energy storage [25]. In our previous study, M. Nicolaescu et al. successfully obtained a flexible negative electrode with high potential for supercapacitor applications prepared via a one-step chemical oxidation process by decorating amorphous ribbons with Fe₂O₃ nanoparticles [26]. Metal oxides can be used both as the anode and cathode materials of supercapacitor devices to provide higher energy densities. Among these metal oxides, CuO, Cu₂O, and Cu₂O/CuO with different structures, including nanowires [27,28], nanorods [29], nanoribbons [30,31], nanowiskers [32], nanoplatelets [33–35], and plate-like nanostructures [36], are attracting considerable interest, due to their environmental friendliness, numerous reserves, low cost, chemical stability, the easy tailoring of various shapes (particularly in nano-dimensions), and excellent electrochemical properties [37].

In recent years, the growth of CuO nano-structures has been developed by various methods, such as the hydrothermal method for the synthesis of well-crystalline CuO nanosheets at a low temperature in large quantities. The morphology and size of CuO nanoparticles can be controlled through adjusting the reaction parameters, i.e., the reactant concentration, precipitant, reaction temperature, and reaction time [38]. H.M. Xiao et al. studied the synthesis of 1D CuO nanorods, 2D flake-like CuO nanostructures, and 3D branch-like CuO nanostructures through a hydrothermal process in the presence of sodium citrate by simply controlling the reaction conditions [39]. The precipitation and sol-gel methods for the synthesis of copper oxide materials are very efficient in producing small-sized nanostructures (less than 2 μm) [40,41]. The micro-emulsion [42], spray pyrolysis [43], and dealloying [44] methods have become very interesting, due to the excellent control of shape, composition, morphology, and use for energy storage application [45]. B. Toboonsung et al. successfully synthesized Cu/CuO nanorods on glass substrates by an electrochemical dissolution and deposition method, observing that the morphology of CuO nanorods depended on the control of the deposition time, electrode separation, and voltage [46]. W. Wang et al. developed uniform CuO nanorods with average diameters of about 8 nm and lengths of up to 400 nm through a novel and simple one-step solid-state reaction in the presence of a suitable surfactant [47]. X. Jiang et al. described a vapor-phase approach to the facial synthesis of cupric oxide (CuO) nanowires supported on the surfaces of various copper substrates that include grids, foils, and wires. A typical procedure simply involved the thermal oxidation of these substrates in the air and within the temperature range of 400 to 700 °C [48].

Above all of these methods, thermal oxidation is one of the simplest top-down strategy techniques for obtaining CuO with different architectures [49]. It involves the formation of CuO nanowires/nanorods/tubes [50] simply by varying the annealing temperatures without the assistance of a catalyst or template. CuO nanowires could be synthesized

by heating Cu foil [51], and the diameter, length, and density of the CuO nanowires have been shown to depend on the heating temperature, treatment time, and substrate nature [52,53]. Obtaining CuO nanowires by thermal oxidation of Cu foil at various heating rates was investigated by L. Nkhaili et al. and successfully electrodeposited on an FTO/glass substrate. The morpho-structural and optical characterization revealed that this simple method is a promising way to improve the surface contact for solar cells and catalytic applications [54]. In this research, a flexible copper mesh oxidized by a one-step thermal oxidation process to grow the Cu₂O/CuO nanowires was used, achieving a positive electrode, namely Cu/Cu₂O/CuO (Nw), for supercapacitor application.

2. Materials and Methods

2.1. Chemicals

The copper mesh (thickness 0.25 mm, wire diameter 0.115 mm), hydrochloric acid (HCl) solution (0.1 M), acetone, and ethyl alcohol were purchased from Sigma-Aldrich Company (St. Louis, MO, USA). All reagents were of analytical grade and used without purification.

2.2. Synthesis Method of the Cu/Cu₂O/CuO (Nw) Electrode

The schematic diagram of the synthesis protocol is illustrated in Figure 1. The Cu/Cu₂O/CuO (Nw) electrode was obtained by using a metal support based on a flexible Cu mesh. The pre-treatment procedure consisted of treating the Cu mesh supports with 0.1 M HCl solution for 30 s to remove the copper oxide layer naturally formed on the surface. Afterwards, the supports were washed intensively several times with acetone, ethyl alcohol, and distilled water in an ultrasonic bath, and finally dried in an oven at 40 °C for 4 h. The final step presumed the thermal treatment of the Cu mesh supports (effective area $1 \times 2 \text{ cm}^2$) into the oven in a controlled atmosphere consisting of a mixed gas flow of Ar (95%) and O₂ (5%), with a gas flow rate of 150 mL min⁻¹ for 4 h at a temperature range of 300 °C to 600 °C. After the thermal oxidation process, the as-obtained Cu/Cu₂O/CuO(Nw) electrodes were kept in hermetically sealed containers.

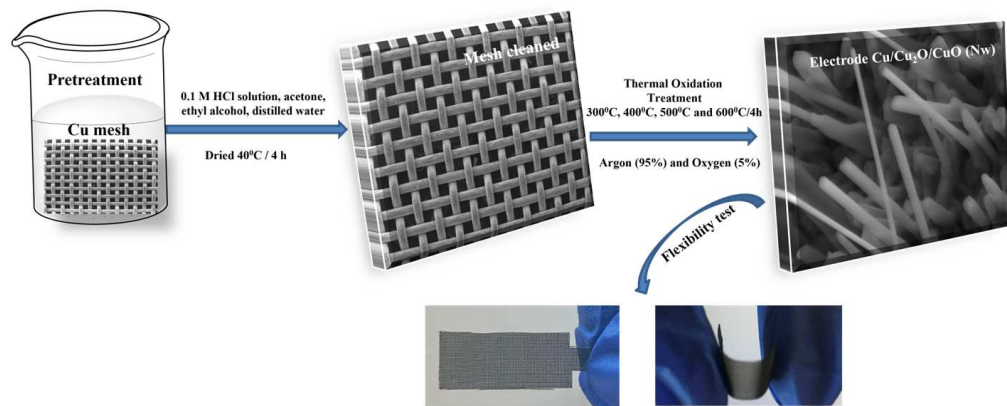


Figure 1. Schematic diagram of the synthesis protocol for the development of the Cu/Cu₂O/CuO (Nw) electrode.

2.3. Cu/Cu₂O/CuO (Nw) Electrodes Characterization

The crystalline structure of the electrodes was evaluated by the X-ray diffraction technique (XRD, PANalytical X’Pert PRO MPD Diffractometer, Almelo, The Netherlands) with Cu-K radiation in the range of $2\theta = 20\text{--}80^\circ$. The microstructure of the samples was analyzed by scanning electron microscopy (SEM, Quanta FEG 250, FEI, Hillsboro, OR, USA) using a secondary electron detector (SE), and the elemental analysis was performed by energy dispersive X-ray spectroscopy (EDX with an Apolo SSD: detector, EDX with an Apolo SSD: detector, EDAX Inc., Mahwah, NJ, USA) to reveal the purity of the materials. To avoid sample charging, the investigations were performed in a low vacuum mode at

a 10 kV voltage using a low kV cone. The chemical analysis was performed at a point of about 10 mm working distance from the sample's surface.

The electrochemical performance of the electrodes was investigated using a classical three-electrode cell system in a 1 M KOH electrolyte solution with a potentiostat/galvanostat (PGSTAT 302, Metrohm Autolab B.V., Utrecht, The Netherlands, controlled with NOVA 2.1 software), with the working electrode Cu/Cu₂O/CuO(Nw) (an effective area of $1 \times 2 \text{ cm}^2$), Ag/AgCl (sat. KCl) as the reference electrode, and platinum wire as the counter electrode. Cyclic voltammetry (CV), galvanostatic charge–discharge (GCD), and electrochemical impedance spectroscopy (EIS) were included as electrochemical measurements.

3. Results and Discussion

3.1. Structural and Morphological Investigations

XRD analysis was used to determine the crystallinity and phase purity of the as-obtained materials for the Cu/Cu₂O/CuO(Nw) electrodes at different oxidation temperatures, as shown in Figure 2. Therefore, all of the peaks observed for the Cu/Cu₂O/CuO (Nw) electrodes presented at 2theta, as follows: at 43.31° , 50.44° , and 74.12° for the cubic phase of Cu (JCPDS card No.: 01-085-1326); at 36.44° , 42.32° , 61.40° , and 73.55° for the cubic phase of Cu₂O (JCPDS card No.: 01-078-2076); and at 35.73° , 38.92° , 49.06° , 61.86° , and 68.50° for the monoclinic phase of CuO (JCPDS card No.: 96-900-8962) confirmed the presence of all of the crystalline phases that occurred after the thermal treatment. When increasing the oxidation temperature, the CuO and Cu₂O peaks were more pronounced, and, according to the literature data, the total transformation of Cu is achieved at a temperature of 1000°C in an oxygen atmosphere for 8 h for the promotion of the growth of pure CuO [55]. In the inset of Figure 1, the percentages of Cu₂O and CuO are shown based on the experimental program. There is an observed linear increase in CuO from 16% to 64% and a corresponding decrease in Cu₂O from 84% to 36%, directly resulting from the experimental conditions. Additionally, it was noticed that, at 500°C , the predominance of the material phases was changed to 54% for CuO and 46% for Cu₂O, compared to 400°C , where the proportions are 34% CuO and 66% Cu₂O.

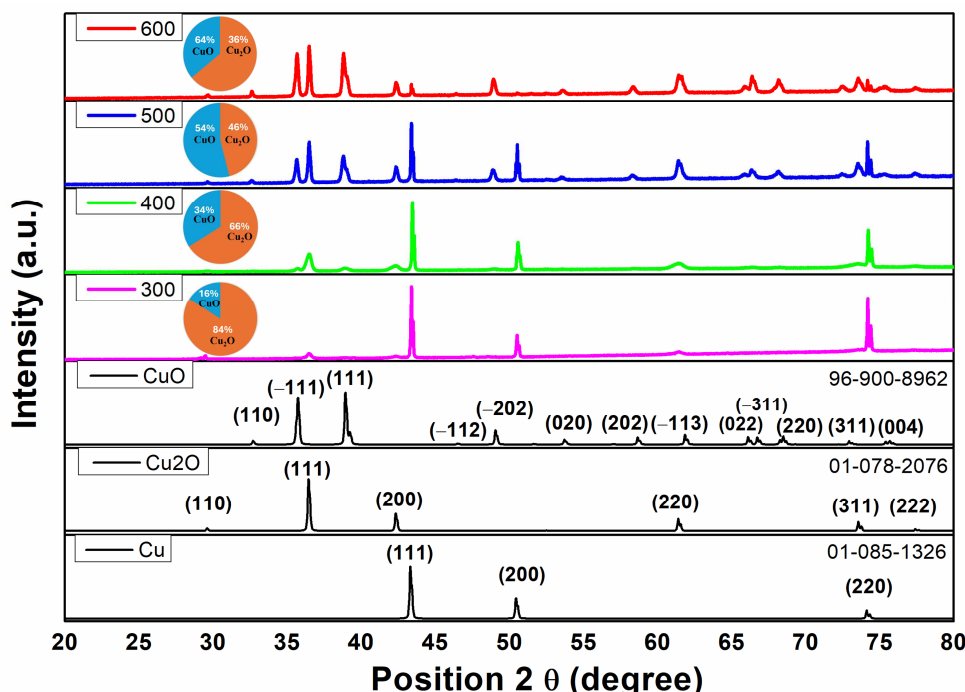


Figure 2. XRD spectra of the as-obtained Cu/Cu₂O/CuO (Nw) electrodes at different oxidation temperatures.

The crystallite sizes (D) of Cu_2O and CuO , obtained using the most intense peak at crystallographic plan (111), have been calculated from the line broadening using Debye–Scherrer's Equation (1), and the values are presented in Table 1.

$$D = K\lambda / \beta \cos\theta \quad (1)$$

where D —crystallite size, K —Scherrer's constant (0.89), λ —X-ray wavelength, θ —Bragg diffraction angle, and β —full width at half maximum (FWHM) of the diffraction peak [56].

Table 1. Crystallite sizes as a function of the oxidation temperature calculated using the Debye–Scherrer's formula. CuO (Nw) average width measured from the SEM image.

Compounds	Crystallite Size/nm			
	300 °C	400 °C	500 °C	600 °C
Cu_2O	23.4	26.4	73.4	110.2
CuO	13.8	14.2	41.7	62.4
Nanowire Average Width/nm				
CuO	29.13	56.85	270.55	437.68

From the data calculated and presented in Table 1, it appears that the crystallite size of CuO is significantly smaller than that of Cu_2O , as expected, the crystallite sizes being directly proportional to the oxidation temperatures.

The SEM morphologies of the electrodes (Figure 3), obtained by thermal oxidation of the copper mesh at different temperatures in a controlled gas atmosphere with a mixed gas flow of Ar and O_2 , show the growth of CuO nanowires for all of the as-synthesized samples but with different densities and widths. Using the imageJ program (Version 1.53t) based on SEM images, raw Cu mesh was measured (Figure 3a) with a dimension of about 0.1 mm wire diameter and $0.15 \times 0.15 \text{ mm}^2$ surface area, and the average nanowire widths of the oxidized samples are presented in Table 1. For all of the samples, it can be seen that most of the CuO nanowires were always almost unidirectional and had grown in a needle shape, i.e., thicker at the bases and thinner at the tips, with the only difference being observed in the width of the wires, which increased proportionally with the oxidation temperature. Based on Figure 3b, for the sample synthesized at 300 °C, it can be seen that the CuO nanowires started to slowly grow on the surface of the Cu mesh, with the average nanowire width being about 29 nm, as presented in Table 1. With the increase in oxidation temperature to 400 °C (Figure 3c), a high density of CuO nanowires was observed, which was correlated with a slight increase in the average widths. Furthermore, at oxidation temperatures of 500 °C and 600 °C (Figure 3d,e), it can be observed that the morphology of the CuO nanowires changed, the density of the nanowires decreased, and their width increased to 430 nm, as seen in Table 1. The change in the morphology of the CuO nanowires proportional to the increase of the oxidation temperature was observed starting from 400 °C (Figure 3c), where the orientation of the nanowires was slightly curved, and, at 600 °C (Figure 3e), the nanowires were almost straight, this aspect being likely due to the difference in the diameter of the nanowires. To confirm the purities of the samples, the EDX analyzes for elemental identification are presented in the Supplementary Materials, Figure S1a–e.

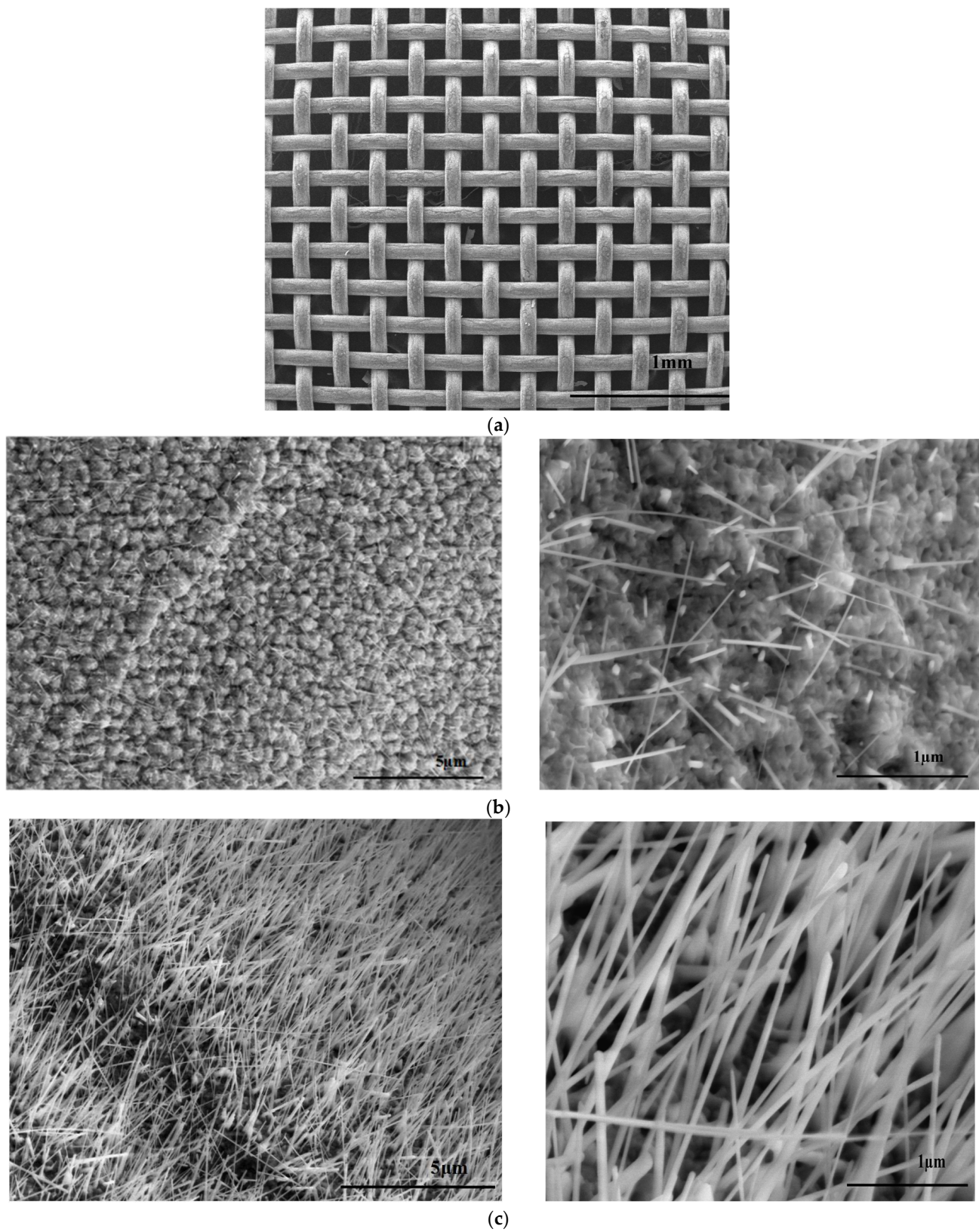


Figure 3. Cont.

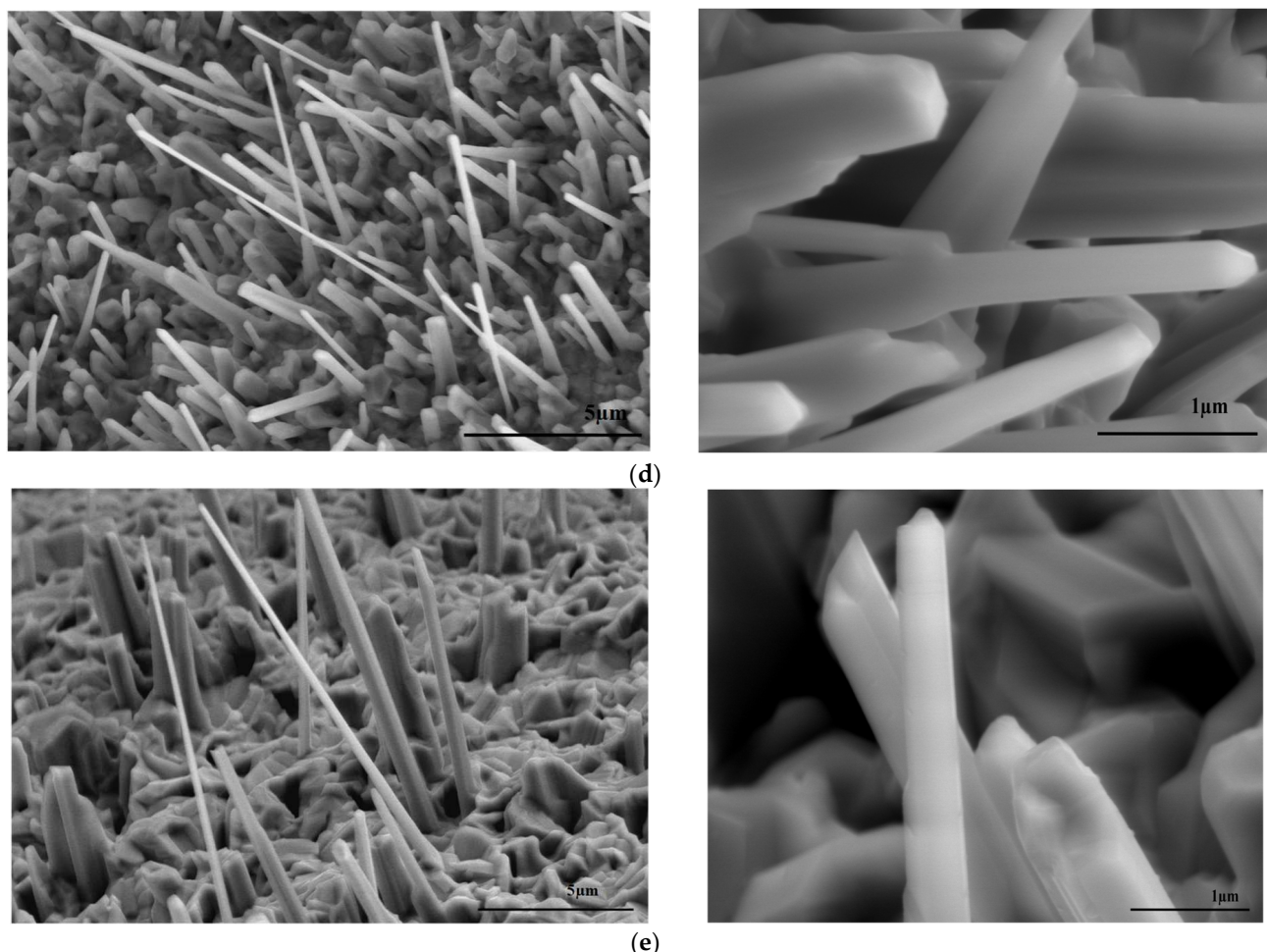


Figure 3. SEM morphologies for raw Cu mesh (a) and for Cu/Cu₂O/CuO (Nw) electrodes oxidized at temperatures of 300 °C (b), 400 °C (c), 500 °C (d), and 600 °C (e).

In an elaborate study by M. Kosicek et al. [57] and L. Nkhaili et al. [54], a mechanism for the formation of CuO nanowires after the thermal oxidation has been presented. Therefore, in the first stage, the process starts with the oxidation of Cu. When a cubic network of Cu₂O is formed, fully ionized oxygen enters the network through the chemisorption process, and the Cu ions that migrate from the Cu/Cu₂O interface to the sample surface, due to boundary diffusion induced by stress, are a continuous source for the formation of nanowires composed of the monoclinic network of CuO. This mechanism was also confirmed in our study by the X-ray patterns presented in Figure 2, where by the thermal oxidation of the Cu mesh for both crystalline phases Cu₂O and CuO were identified.

3.2. Electrochemical Performance of the Cu/Cu₂O/CuO (Nw) Electrodes

The electrochemical behavior of the Cu/Cu₂O/CuO(Nw) electrodes was investigated at various experimental conditions using cyclic voltammetry (CV), as presented in Figure 4a–d. A potential window of 0 to 0.6 V was selected, in accordance with previous studies [58], and the measurements were conducted at scan rates of 5, 10, 20, 50, and 100 mV s⁻¹, revealing positive electrode behavior. Based on the CV experiments, the current increased with higher scan rates, indicating the capacitive nature of the electrodes. The presence of unclear oxidation peaks and a broad reduction peak resulted in non-rectangular CV curves, attributed to the quasi-reversible faradaic process [59,60]. Additionally, slight variations in the shape of the CV curve were observed, depending on the experimental parameters, offering valuable insights into the charge storage mechanisms and the electrode performance [45].

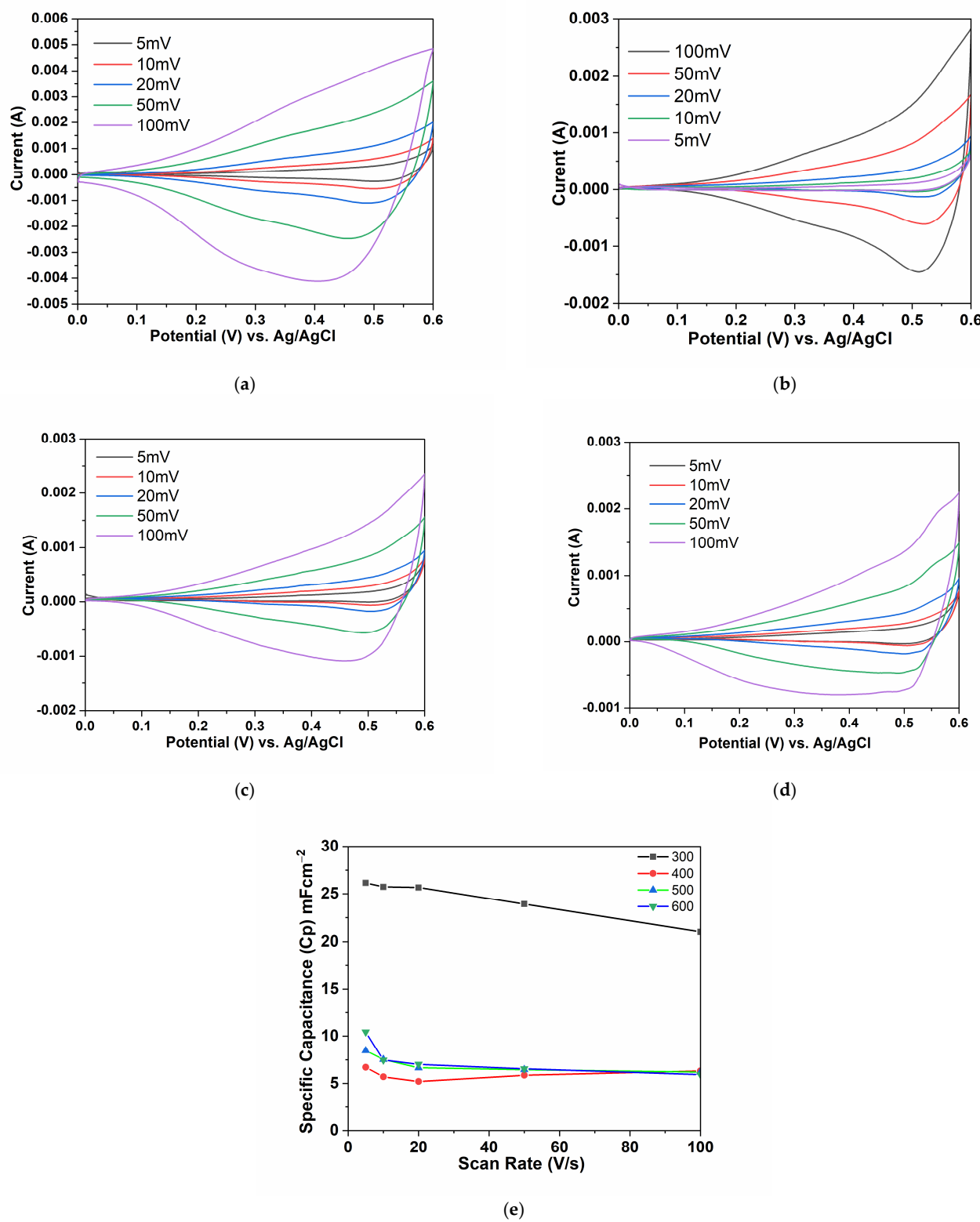
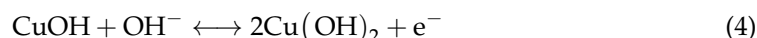
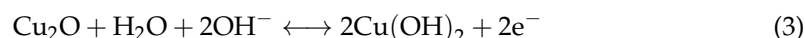
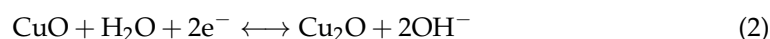


Figure 4. Cyclic voltammograms recorded for Cu/Cu₂O/CuO (Nw) electrodes obtained by thermal oxidation at 300 °C (a), 400 °C (b), 500 °C (c), and 600 °C (d). Plots of specific capacitance vs. potential scan rate of the electrodes (e).

Notably, in the case of the Cu/Cu₂O/CuO(Nw) positive electrode, the CV curves displayed a non-ideal rectangular shape, suggesting the presence of pseudo-capacitance in the electrode material. However, at an oxidation temperature of 600 °C (Figure 4d), more

pronounced reduction and oxidation peaks were evident, which indicated an increased faradaic process with a higher oxidation temperature. The non-linear relationship between the current and the potential responses further supported the existence of faradaic pseudo-capacitance, with slight variations depending on the experimental conditions [61]. Pseudo-capacitance involves reversible redox reactions of the metal oxide, with electron transfer between the electrode and the ions in the electrolyte. These reactions lead to the intercalation (insertion) and deintercalation (extraction) of ions into and out of the metal oxide structure, storing charge in the process, as presented in Equations (2)–(5), as follows:



The redox reactions that occur during charging (Equations (2) and (3)) are reversed during discharging. The copper oxide returns to its original oxidation state, releasing the electrons and ions back into the electrolyte. For example, $\text{Cu}(\text{OH})_2$ transforms back into CuO , releasing protons (H^+) and electrons (e^-). Similarly, Cu and H_2O transform back into Cu_2O , releasing protons and electrons (Equations (4) and (5)).

Overall, these aspects underline the complex electrochemical behavior of the $\text{Cu}/\text{Cu}_2\text{O}/\text{CuO}(\text{Nw})$ electrodes characterized by a combination of capacitive and faradaic processes, influenced by factors such as the scan rate and the oxidation temperature [45].

The capacitance (C_p) from the CV analysis was calculated dependent of the scan rate and proportional with the area, according to Equation (6) [24,62], as follows:

$$C_p = \frac{A}{kS\Delta V} \quad (6)$$

where A —area under the curve, k —scan rate, S —area of the active material (cm^2), and ΔV —potential window.

The calculated capacitance versus the scan rate of the CV analysis for all positive electrodes is plotted in Figure 4e. The highest capacitance values were achieved at a scan rate of 5 mV s^{-1} , measuring $26.158 \text{ mF cm}^{-2}$ for the 300°C electrode, 6.704 mF cm^{-2} for the 400°C electrode, 8.457 mF cm^{-2} for the 500°C electrode, and $10.441 \text{ mF cm}^{-2}$ for the 600°C electrode. A non-regular behavior can be observed, which was likely due to the irregular crystal growth behavior of the CuO nanowires at 400°C compared to the other experimental parameters [45,61]. Additionally, the higher capacitance observed at the 300°C electrode may be attributable to the more efficient process that occurs when the nanowires are smaller, potentially due to the higher surface area achieved when the wires are small [63]. A decrease in specific capacitance was observed with increasing scan rates, however, due to variations in the experimental parameters, the rate of decrease varied across the different electrodes. This indicates that electrons have different diffusion rates compared to ions. The charge storage capacity decreased the most for the 600°C electrode, with a reduction of 43.29%, and the 500°C and 300°C electrodes showed reductions of 25.5% and 19.6%, respectively. For the 400°C electrode, the decrease was only 5.82%. The redox reaction responsible for the pseudo-capacitive behavior of $\text{Cu}/\text{Cu}_2\text{O}/\text{CuO}(\text{Nw})$ is based on the diffusion of ions from the electrolyte into the active materials. In our case, the higher density of the copper oxide nanowires decreased the efficiency of the intercalation deintercalation process between the ions [63]. Consequently, as the nanowires grew, only a small fraction of the electrode material could be effectively utilized, while most of the material remained unutilized at higher scan rates [64]. To assess the flexibility of the electrode, CV tests were performed within the potential window range of 0 to 0.6 V at the

following bending angles: 0°, 45°, 90°, 135°, and 180°, using a scan rate of 100 mV s⁻¹, as shown in Figure S2. The bending analysis was conducted consecutively, with the angles being manually adjusted. The results showed that the surface area of the CV curves increased as the bending angles increased, which generated an increase in capacitance. At a bending angle of 45°, the capacity retention was 125.6%, which increased to 139.84% for 90°. This retention increased linearly to 156.96% and 167.95% at bending angles of 135° and 180°, respectively. These results indicate that the electrode is suitable for use in flexible supercapacitors.

The performance of the Cu/Cu₂O/CuO(Nw) positive electrodes presented in Figure 5a–d shows the galvanostatic charge–discharge (GCD) curves plotted against time for various current densities (0.5, 1, 2, 4, and 8 mA cm⁻²). As evidenced in all of the GCD experiments, there is a consistent trend suggesting that, as the current density increases, the discharging time for the positive electrodes decreases. This observation aligns with the behavior typically seen in other supercapacitor materials [60]. Furthermore, the GCD curves display an asymmetric or nonlinear (quasi-triangular) shape, presenting three variations during the discharging process [65]. This non-uniform shape indicates a pseudo-capacitive behavior within the positive electrode, confirming the conclusions from the CV measurements of the copper oxide electrodes. In addition, the charging segments were nearly symmetric to their corresponding discharging counterparts, indicating the excellent reversibility of the Cu/Cu₂O/CuO(Nw) positive electrode [66,67]. To assess the pseudo-capacitive behavior of the Cu/Cu₂O/CuO(Nw) positive electrode, the discharge region was typically examined for precise data. This region of the GCD curve comprises three primary domains, as follows: an initial rapid voltage drop (due to internal resistance, IR); followed by an exponential voltage variation over time, indicative of the material's pseudo-capacitance behavior; and, finally, a third region attributed to Faradaic processes, such as redox reactions or electrochemical adsorption/desorption occurring at the electrode–electrolyte interface [66].

It is interesting to notice the presence of IR drops depending on the experimental parameters, indicating slight variations in the internal resistance between the electrodes. The significant IR drop observed at 400 °C suggests that the morpho-structural properties of the CuO nanowires may enhance the conductivity, particularly at lower current densities of the electrode material [68]. This observation helps to explain the irregularities in the capacitance, which is in accordance with the data from the CV measurements.

Figure 5e shows the specific capacitance (C_{SP}) of the Cu/Cu₂O/CuO (Nw) electrodes, which was calculated from the GCD analysis and plotted against the current density following Equation (7) [24,62], as follows:

$$C_{SP} = I \Delta t / \Delta V S \quad (7)$$

where, I—applied current (mA); Δt —discharge time in seconds (s); ΔV —discharge voltage in volts (V); and S—the area of the active material (cm²).

Overall, the highest capacitance values were achieved at the lowest current density of 0.5 mA cm⁻² for all of the electrodes. The highest value was calculated at 21.198 mF cm⁻² for the oxidation temperature of 300 °C, followed by a decrease in capacitance to 7.903 mF cm⁻² for 400 °C. There was a slight increase to 8.727 mF cm⁻² for the temperature of 500 °C, followed by another decrease to 6.981 mF cm⁻² for the temperature of 600 °C. This irregular behavior can be attributed to the different mechanisms observed in the GCD analysis at lower current densities [45]. At lower current densities, the plot displays varying IR drops and proportions of pseudo-capacitive to Faradaic redox reactions at the interface because of the morphological and structural differences in the nanowires [66]. However, at higher current densities (>2 mA cm⁻²), the plot assumed a more triangular shape, indicating a reduced role of the redox reaction in the overall mechanism of the interface and, consequently, leading to an experimental decrease in behavior [45].

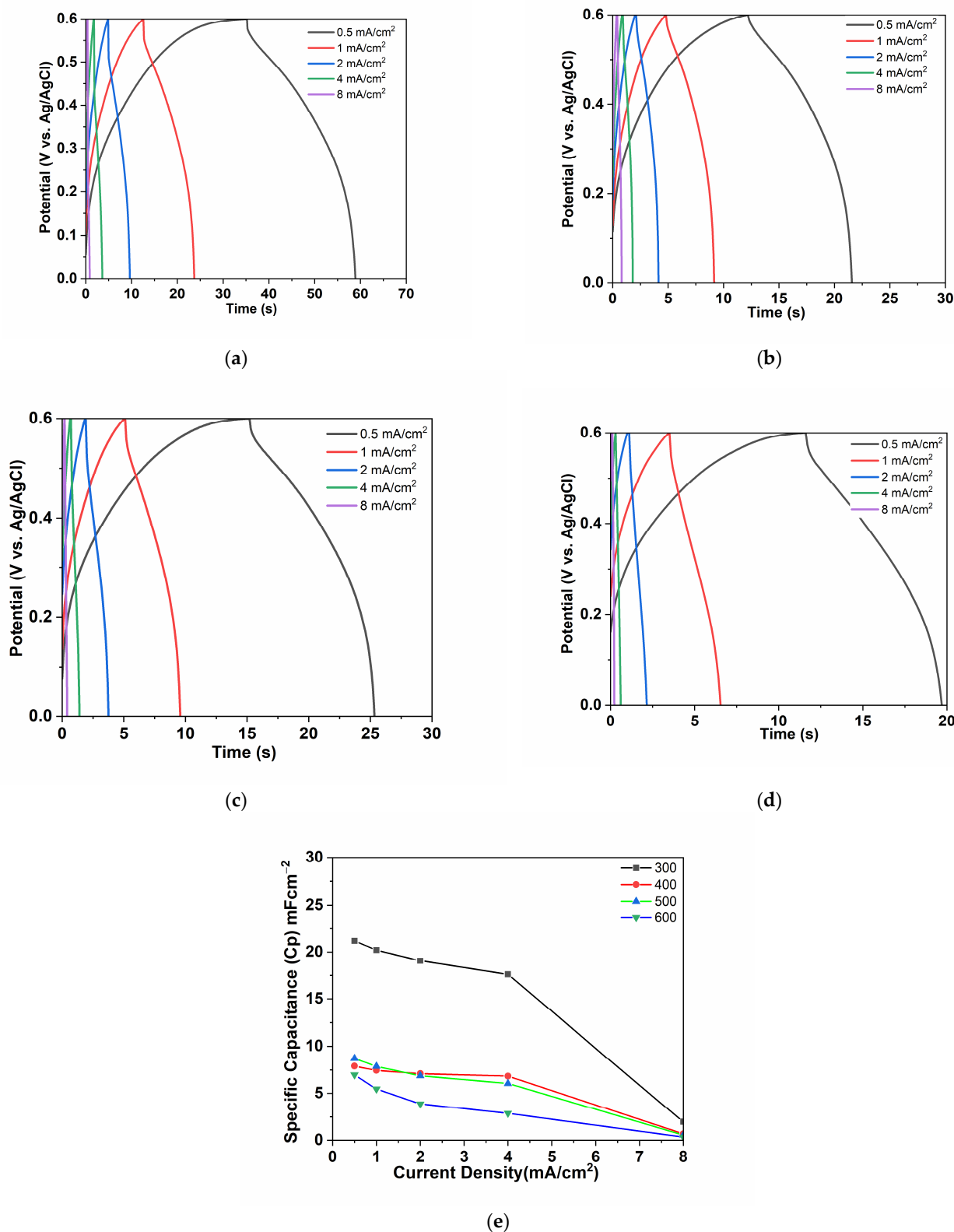


Figure 5. GCD curves of Cu/Cu₂O/CuO (Nw) electrodes obtained by thermal oxidation at 300 °C (a), 400 °C (b), 500 °C (c), and 600 °C (d). Specific capacitance vs. current density for all as-obtained electrodes (e).

In a research study, A. Lamberti et al. [58], suggested that the growth of nanowires enables an increase in the surface area and enhances the electrochemical activity for charge storage. However, in our study, the nanowires tended to grow more due to the experi-

mental parameters and an increased experimental duration. As a result, our experiments demonstrate that smaller copper wires are more suitable for supercapacitor applications. It is likely that the capacitance increases exponentially up to a certain level, but, when the wires become too large, the useful surface area decreases, leading to a drop in capacitance.

The cycling stability of all of the as-obtained Cu/Cu₂O/CuO (Nw) electrodes at a current density of 8 mA cm⁻², presented in Figure 6a, was evaluated over 500 cycles using GCD analysis. All of the electrodes exhibited a relatively long cycle life at 8 mA cm⁻², confirming their electrochemical stability from the evaluation of the specific capacitance values presented in Figure 6b. Interestingly, except for the sample treated at 600 °C, which showed a slight decrease in capacitance over time, the Cu/Cu₂O/CuO (Nw) electrodes displayed a gradual increase in capacitance over the cycles, with a noticeable peak in capacitance at 400 cycles, followed by a very slight decrease in capacitance over the last 100 cycles. For 500 cycles, the electrode treated at 300 °C demonstrated a retention rate of 110.35%, 134.06% for the 400 °C electrode, and 115.39% for the 500 °C electrode. However, for the electrode treated at 600 °C, there was a reduction in the retention rate to 96.98% from the initial value. The maximum retention rate was observed for the 400 °C electrode, reaching 156.52% at 400 cycles. The observed increase in capacitance after cycling is likely attributable to the complete activation of the transition metal oxide Cu₂O/CuO (Nw) from the copper mesh electrode [24]. This activation process involves the repeated intercalation and deintercalation of the electrolyte ions, along with the gradual insertion of the electrolyte into the bulk structure of the Cu₂O/CuO (Nw). Consequently, additional electrochemical active sites were created, contributing to the observed increase in capacitance during the cycling process.

Table 2 summarizes the specific capacitance studies reported for the different structures of copper oxide electrodes used for supercapacitor applications. Within our proposed research, many advantages, such as a low production cost, high reproducibility, and no use of hazardous chemicals, were evidenced. Moreover, the use of a metal substrate, such as copper mesh, in the realization of supercapacitor devices is a favorable approach, not only for enhancing the electrochemical properties, but also for simplifying the design of the electrode materials.

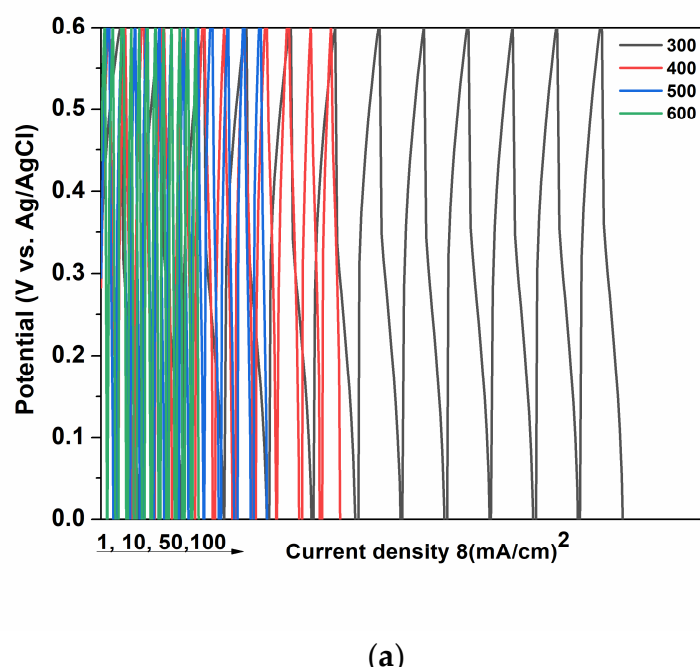
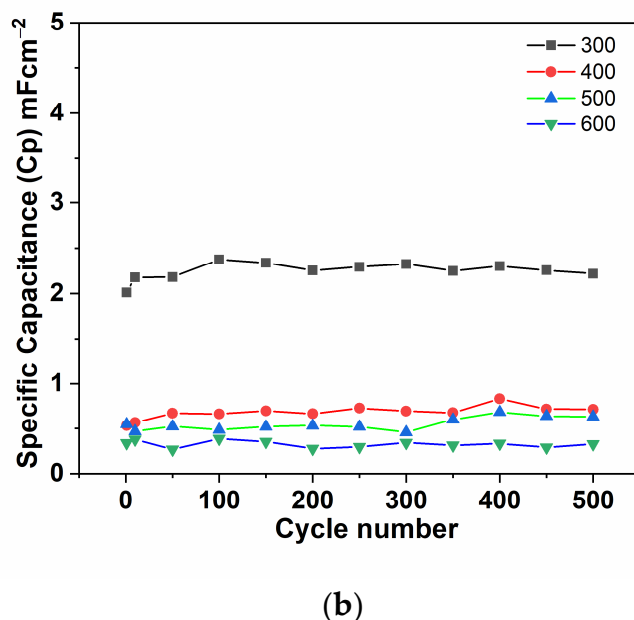


Figure 6. Cont.



(b)

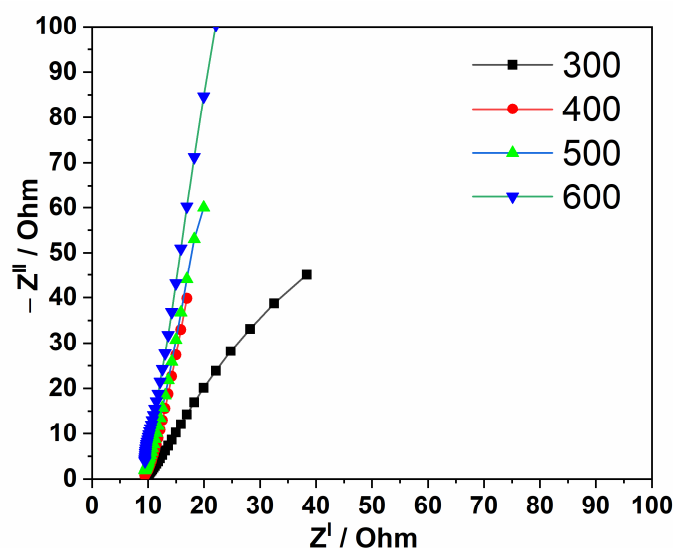
Figure 6. (a) GCD curves in accordance with cycling stability and (b) specific capacitance at 500 cycles of the as-obtained Cu/Cu₂O/CuO (Nw) electrodes at a current density of 8 mA cm⁻².

Table 2. Different structures of the CuO electrodes used for supercapacitor application.

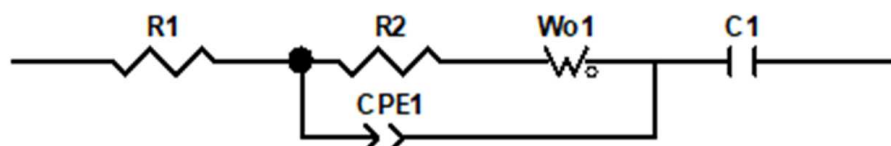
Materials	Structure	Specific Capacitance	Scan Rate	Specific Capacitance	Current Density	References
3D CuO/Cu flowers	Electrode	-	-	3348.57 mF cm ⁻²	1 mA cm ⁻²	[69]
CuO-Cu ₂ O	Nanocomposite Electrode	1954 mF cm ⁻²	2 mV s ⁻¹	-	-	[70]
Cu ₂ O/CuO@Cu-CCs	Electrode	-	-	1710 mF cm ⁻²	10 mA cm ⁻²	[1]
Cu ₂ O/CuO	Composite Electrode	-	-	1280 mF cm ⁻²	40 mA cm ⁻²	[71]
CuO	Nanostructured Electrode	231 mF cm ⁻²	2 mV s ⁻¹	-	-	[61]
Copper hydroxide nanostructures	Electrode	42 mF cm ⁻²	20 mV s ⁻¹	-	-	[72]
Cu ₂ O/Cu columnar array	Electrode	128.6 mF cm ⁻²	5 mV s ⁻¹	-	-	[73]
NiMoO ₄ NSs-CNTs-CuO NWAs/Cu foam	Electrode	-	-	23.40 F cm ⁻²	2 mA cm ⁻²	[74]
Cu/Cu ₂ O/CuO (Nw)	Electrode	26.158 mF cm ⁻²	5 mV s ⁻¹	21.198 mF cm ⁻²	0.5 mA cm ⁻²	This work

Electrochemical impedance spectroscopy (EIS) over a frequency range of 0.1 Hz to 10.000 Hz, with an amplitude of 0.01 V, was recorded for all of the experimental Cu/Cu₂O/CuO (Nw) electrodes and is presented in Figure 7a. The EIS spectra are divided into three distinct regions based on decreasing frequencies. In the low-frequency range, the slope of the EIS curve represents Warburg resistance, which characterizes the diffusion rates of the redox material in the electrolyte [67]. The electrodes registering values higher than 45° in this range indicate diffusion-controlled electrochemical capacitive behavior [75]. The semicircle observed at high frequencies symbolizes the charge-transfer resistance (R_P) that

occurs due to ion diffusion between the electrode material and the electrolyte. Figure 7b displays the equivalent circuit used for curve fitting and the resulting values. A linear relationship between the resistance and the experimental parameters was observed, likely attributable to the surface morphology and variations in the nanowire size [75]. The R_p value for the electrodes oxidized at a temperature of 300 °C was about 2.5 Ω, which is lower than that for the 400, 500, and 600 °C electrodes, which increased to 3.2 Ω, 4.4 Ω, and 10 Ω, respectively. This further indicates that smaller nanowire structures are superior because of increased conductivity, resulting in higher capacitance due to faster ion and electron transport [67,76]. The intercept on the real axis (where the impedance is zero) in the high-frequency range represents the ohmic resistance of the electrode–electrolyte interface (R_s), calculated according to the circuit depicted in Figure 7b [24]. The values of R_s for the electrodes at 300 °C, 400 °C, 500 °C, and 600 °C were determined to be 9.1 Ω, 4.0 Ω, 4.6 Ω, and 5 Ω, respectively. The low value of 4.0 Ω for the 400 °C electrode explains the minimal I_R drops observed in the GCD analysis [45].



(a)



(b)

Figure 7. Nyquist plots of all as-obtained Cu/Cu₂O/CuO (Nw) electrodes (a). Simulation of the equivalent circuit fitting of the electrodes (b).

4. Conclusions

Cu/Cu₂O/CuO(Nw) positive electrodes for supercapacitor application by one-step thermal oxidation using a flexible copper mesh were successfully assessed within this study. The growth of Cu₂O/CuO nanowires occurred within a temperature oxidation range of 300 to 600 °C in a controlled atmosphere of Ar and O₂ mixed-flow gases, with SEM morphology confirming the presence of nanowires, and based on the average widths, the measurements started from 29 nm at 300 °C to 430 nm at 600 °C. The crystalline phases and material purity were confirmed by XRD and EDX analysis. As expected, the crystallite sizes calculated by Debye–Scherrer's formula for CuO were significantly smaller than those of Cu₂O. This is likely because CuO is copper (II) oxide and forms after Cu₂O. The electrochemical analysis

revealed that the Cu/Cu₂O/CuO(Nw) electrodes function as positive electrodes. The highest capacitance values obtained from the CV analysis were observed at a scan rate of 5 mV s⁻¹, measuring 26.158 mF cm⁻² for the electrode prepared at 300 °C. To assess the flexibility of the electrodes, CV curves were recorded at various bending angles, including 0°, 45°, 90°, 135°, and 180°, demonstrating that the specific capacitance increased with the bending angles. The GCD analysis indicated that the maximum specific capacitance of 21.198 mF cm⁻² was achieved at a low power density of 0.5 mA cm⁻², as for the 300 °C electrode. The GCD cycle analysis revealed a maximum retention rate of 156.52% at 400 cycles, indicating that the electrode's capacitance value increased by 56.52% from its initial capacitance. Furthermore, the EIS analysis demonstrated that all of the electrodes exhibited favorable capacitive behavior, as evidenced by a 45-degree inclination with a decrease in frequency.

Supplementary Materials: The following supporting information can be downloaded at: <https://www.mdpi.com/article/10.3390/batteries10070246/s1>, Figure S1. EDX analysis for elemental identification of raw Cu mesh (a) and, for Cu/Cu₂O/CuO (Nw) electrodes oxidized at temperatures of 300 °C (b); 400 °C (c); 500 °C (d); 600 °C (e) and Figure S2. CV curves of Cu/Cu₂O/CuO (Nw) electrode obtained at 300 °C at different bent angles for flexibility evaluation. Inset: Picture of bending angle = 90°.

Author Contributions: Conceptualization, M.-I.M., M.N., N.D., C.O. and C.B.; methodology, M.N., C.B. and C.L.; validation, N.D., C.L. and C.B.; investigation, M.-I.M., M.N., I.H. and C.O.; writing—original draft preparation, M.N., N.D., C.O., C.L. and C.B.; writing—review and editing, C.L. and C.B.; visualization, C.L. and C.B.; supervision, C.L. and C.B. All authors have read and agreed to the published version of the manuscript.

Funding: This research was funded by a grant from the Ministry of Research, Innovation, and Digitization, project number PN-IV-P8-8.3-ROMD-2023-0227, within PNCDI IV, and partially by the project code PN 23 27 01 02 INOMAT, 23-27 29N/2023.

Data Availability Statement: The data presented in this study are available on request from the corresponding author.

Conflicts of Interest: The authors declare no conflicts of interest.

References

- Xu, L.; Li, J.; Sun, H.; Guo, X.; Xu, J.; Zhang, H.; Zhang, X. In situ growth of Cu₂O/CuO nanosheets on Cu coating carbon cloths as a binder-free electrode for asymmetric supercapacitors. *Front. Chem.* **2019**, *7*, 420. [[CrossRef](#)] [[PubMed](#)]
- Wei, D.; Scherer, M.R.; Bower, C.; Andrew, P.; Ryhänen, T.; Steiner, U. A nanostructured electrochromic supercapacitor. *Nano Lett.* **2012**, *12*, 1857–1862. [[CrossRef](#)] [[PubMed](#)]
- Kiruthika, S.; Kulkarni, G.U. Smart electrochromic supercapacitors made of metal mesh electrodes with polyaniline as charge storage indicator. *Energy Technol.* **2020**, *8*, 1901364. [[CrossRef](#)]
- Kim, D.Y.; Ghodake, G.S.; Maile, N.C.; Kadam, A.A.; Sung Lee, D.; Fulari, V.J.; Shinde, S.K. Chemical synthesis of hierarchical NiCo₂S₄ nanosheets like nanostructure on flexible foil for a high performance supercapacitor. *Sci. Rep.* **2017**, *7*, 9764. [[CrossRef](#)] [[PubMed](#)]
- Chen, X.; Liu, X.; Liu, Y.; Zhu, Y.; Zhuang, G.; Zheng, W.; Cai, Z.; Yang, P. Advanced binder-free electrodes based on CoMn₂O₄ @Co₃O₄ core/shell nanostructures for high-performance supercapacitors. *RSC Adv.* **2018**, *8*, 31594–31602. [[CrossRef](#)] [[PubMed](#)]
- Guo, N.; Wei, X.Q.; Deng, X.L.; Xu, X.J. Synthesis and property of spinel porous ZnMn₂O₄ microspheres. *Appl. Surf. Sci.* **2015**, *356*, 1127–1134. [[CrossRef](#)]
- Chiam, S.L.; Lim, H.N.; Hafiz, S.M.; Pandikumar, A.; Huang, N.M. Electrochemical performance of supercapacitor with stacked copper foils coated with graphene nanoplatelet. *Sci. Rep.* **2018**, *8*, 3093. [[CrossRef](#)] [[PubMed](#)]
- Aouini, S.; Bardaoui, A.; Santos, D.M.F.; Chtourou, R. Hydrothermal synthesis of CuMn₂O₄ spinel-coated stainless steel mesh as a supercapacitor electrode. *J. Mater. Sci. Mater. Electron.* **2022**, *33*, 12726–12733. [[CrossRef](#)]
- Wang, W.; Guo, S.; Lee, I.; Ahmed, K.; Zhong, J.; Favors, Z.; Francisco, Z.; Mihrimah, O.; Ozkan, C.S. Hydrous ruthenium oxide nanoparticles anchored to graphene and carbon nanotube hybrid foam for supercapacitors. *Sci. Rep.* **2014**, *4*, 4452. [[CrossRef](#)] [[PubMed](#)]
- Ouyang, Y.; Huang, R.; Xia, X.; Ye, H.; Jiao, X.; Wang, L.; Lei, W.; Hao, Q. Hierarchical structure electrodes of NiO ultrathin nanosheets anchored to NiCo₂O₄ on carbon cloth with excellent cycle stability for asymmetric supercapacitors. *Chem. Eng. J.* **2019**, *355*, 416–427. [[CrossRef](#)]

11. Kim, S.W.; Kim, I.H.; Kim, S.I.; Jang, J.H. Nickel hydroxide supercapacitor with a theoretical capacitance and high rate capability based on hollow dendritic 3D-nickel current collectors. *Chem. Asian J.* **2017**, *12*, 1291–1296. [[CrossRef](#)] [[PubMed](#)]
12. Zan, G.; Li, S.; Chen, P.; Dong, K.; Wu, Q.; Wu, T. Mesoporous Cubic Nanocages Assembled by Coupled Monolayers With 100% Theoretical Capacity and Robust Cycling. *ACS Cent. Sci.* **2024**, *10*, 1283–1294. [[CrossRef](#)] [[PubMed](#)]
13. Han, C.; Xu, X.; Mu, H.; Tian, Q.; Li, Q.; Liu, Y.; Zhang, X.; Zhao, Z.; Su, X. Construction of hierarchical sea urchin-like manganese substituted nickel cobaltite@tricobalt tetraoxide core-shell microspheres on nickel foam as binder-free electrodes for high performance supercapacitors. *J. Colloid Interface Sci.* **2021**, *596*, 89–99. [[CrossRef](#)] [[PubMed](#)]
14. Huang, M.; Li, F.; Dong, F.; Zhang, Y.; Zhang, L.L. MnO₂-based nanostructures for high-performance supercapacitors. *J. Mater. Chem. A* **2015**, *3*, 21380–21423. [[CrossRef](#)]
15. Liu, T.; Zhang, L.; You, W.; Yu, J. Core-shell nitrogen-doped carbon hollow spheres/Co₃O₄ nanosheets as advanced electrode for high performance supercapacitor. *Small* **2018**, *14*, 1702407. [[CrossRef](#)] [[PubMed](#)]
16. Yang, W.; Qu, G.; Chen, M.; Ma, W.; Li, W.; Tang, Y. Effective NaBH₄-exfoliated ultrathin multilayer Co(OH)₂ nanosheets arrays and sulfidation for energy storage. *Nanotechnology* **2018**, *29*, 295403. [[CrossRef](#)]
17. Foo, C.Y.; Sumboja, A.; Tan, D.J.H.; Wang, J.; Lee, P.S. Flexible and highly scalable V₂O₅-rGO electrodes in an organic electrolyte for supercapacitor devices. *Adv. Energy Mater.* **2014**, *4*, 1400236. [[CrossRef](#)]
18. Bu, I.Y.Y.; Huang, R. Fabrication of CuO-decorated reduced graphene oxide nanosheets for supercapacitor applications. *Ceram. Int.* **2017**, *43*, 45–50. [[CrossRef](#)]
19. Li, Y.; Wang, X.; Yang, Q.; Javed, M.S.; Liu, Q.; Xu, W.; Hu, C.; Wei, D. Ultra-fine CuO nanoparticles embedded in three-dimensional graphene network nanostructure for high-performance flexible supercapacitors. *Electrochim. Acta* **2017**, *234*, 63–70. [[CrossRef](#)]
20. Liu, Y.; Cao, X.; Jiang, D.; Jia, D.; Liu, J. Hierarchical CuO nanorod arrays in situ generated on three-dimensional copper foam via cyclic voltammetry oxidization for high-performance supercapacitors. *J. Mater. Chem. A* **2018**, *6*, 10474–10483. [[CrossRef](#)]
21. Zhang, W.; Yin, Z.; Chun, A.; Yoo, J.; Diao, G.; Kim, Y.S.; Piao, Y. Rose rock-shaped nano Cu₂O anchored graphene for high-performance supercapacitors via solvothermal route. *J. Power Sources* **2016**, *318*, 66–75. [[CrossRef](#)]
22. Ji, Y.; Liu, J.; Liu, X.; Yuen, M.M.F.; Fu, X.Z.; Yang, Y.; Sun, R.; Wong, C.P. 3D porous Cu@Cu₂O films supported Pd nanoparticles for glucose electrocatalytic oxidation. *Electrochim. Acta* **2017**, *248*, 299–306. [[CrossRef](#)]
23. Vidyadharan, B.; Misnon, I.I.; Ismail, J.; Yusoff, M.M.; Jose, R. High performance asymmetric supercapacitors using electrospun copper oxide nanowires anode. *J. Alloys Compd.* **2015**, *633*, 22–30. [[CrossRef](#)]
24. Bandas, C.; Nicolaescu, M.; Popescu, M.I.; Orha, C.; Căprărescu, S.; Lazau, C. One-step microwave-assisted hydrothermal preparation of Zn-ZnO(Nw)-rGO electrodes for supercapacitor applications. *Materials* **2023**, *16*, 4536. [[CrossRef](#)] [[PubMed](#)]
25. Yavuz, A.; Kaplan, K.; Bedir, M. Copper oxide coated stainless steel mesh for flexible electrodes. *J. Phys. Chem. Solids* **2021**, *150*, 109824. [[CrossRef](#)]
26. Nicolaescu, M.; Vajda, M.; Lazau, C.; Orha, C.; Bandas, C.; Serban, V.A.; Codrean, C. Fabrication of flexible supercapacitor electrode materials by chemical oxidation of iron-based amorphous ribbons. *Materials* **2023**, *16*, 2820. [[CrossRef](#)] [[PubMed](#)]
27. Su, Y.K.; Shen, C.M.; Yang, H.T.; Li, H.L.; Gao, H.J. Controlled synthesis of highly ordered CuO nanowire arrays by template-based sol-gel route. *Trans. Nonferrous Met. Soc. China* **2007**, *17*, 783. [[CrossRef](#)]
28. Chen, J.T.; Zhang, F.; Wang, J.; Zhang, G.A.; Miao, B.B.; Fan, X.Y.; Yan, D.; Yan, P.X.J. CuO nanowires synthesized by thermal oxidation route. *J. Alloys Compd.* **2008**, *454*, 268–273. [[CrossRef](#)]
29. Yao, W.T.; Yu, S.H.; Zhou, Y.; Jiang, J.; Wu, Q.S.; Zhang, L.; Jiang, J. Formation of uniform CuO manorods by spontaneous aggregation: selective synthesis of CuO, Cu₂O, and Cu nanoparticles by a solid–liquid phase arc discharge process. *J. Phys. Chem. B* **2005**, *109*, 14011–14016. [[CrossRef](#)] [[PubMed](#)]
30. Zhu, C.L.; Chen, C.N.; Hao, L.Y.; Hu, Y.; Chen, Z.Y. In-situ preparation of 1D CuO nanostructures using Cu₂(OH)₂CO₃ nanoribbons as precursor for sacrifice-template via heat-treatment. *J. Cryst. Growth* **2004**, *263*, 473. [[CrossRef](#)]
31. Gou, X.; Wang, G.; Yang, J.; Park, J.; Wexler, D. Chemical synthesis, characterisation and gas sensing performance of copper oxide nanoribbons. *J. Mater. Chem.* **2008**, *18*, 965–969. [[CrossRef](#)]
32. Qu, Y.; Li, X.; Chen, G.; Zhang, H.; Chen, Y. Synthesis of Cu₂O nano-whiskers by a novel wet-chemical route. *Mater. Lett.* **2008**, *62*, 886–888. [[CrossRef](#)]
33. Liu, Y.; Chu, Y.; Li, M.; Li, L.; Dong, L. In situ synthesis and assembly of copper oxide nanocrystals on copper foil via a mild hydrothermal process. *J. Mater. Chem.* **2006**, *16*, 192–198. [[CrossRef](#)]
34. Vaseem, M.; Umar, A.; Hahn, Y.B.; Kim, D.H.; Lee, K.S.; Jang, J.S.; Lee, J.S. Flower-shaped CuO nanostructures: Structural, photocatalytic and XANES studies. *Catal. Commun.* **2008**, *10*, 11–16. [[CrossRef](#)]
35. Volanti, D.P.; Keyson, D.; Cavalcante, L.S.; Simões, A.Z.; Joya, M.R.; Longo, E.; Varela, J.A.; Pizani, P.S.; Souza, A.G. Synthesis and characterization of CuO flower-nanostructure processing by a domestic hydrothermal microwave. *J. Alloys Compd.* **2008**, *459*, 537–542. [[CrossRef](#)]
36. Li, Y.; Liang, J.; Tao, Z.; Chen, J. CuO particles and plates: Synthesis and gas-sensor application. *Mater. Res. Bull.* **2008**, *43*, 2380–2385. [[CrossRef](#)]
37. Chen, A.; Long, H.; Li, X.; Li, Y.; Yang, G.; Lu, P. Controlled growth and characteristics of single-phase Cu₂O and CuO films by pulsed laser deposition. *Vacuum* **2009**, *83*, 927–930. [[CrossRef](#)]

38. Jia, W.; Reitz, E.; Shimpi, P.; Rodriguez, E.G.; Gao, P.-X.; Lei, Y. Spherical CuO synthesized by a simple hydrothermal reaction: Concentration-dependent size and its electrocatalytic application. *Mater. Res. Bull.* **2009**, *44*, 1681–1686. [CrossRef]
39. Xiao, H.-M.; Fu, S.-Y.; Zhu, L.-P.; Li, Y.-Q.; Yang, G. Controlled synthesis and characterization of CuO nanostructures through a facile hydrothermal route in the presence of sodium citrate. *Eur. J. Inorg. Chem.* **2007**, *14*, 1966–1971. [CrossRef]
40. Saadaldin, N.; Alsloum, M.N.; Hussain, N. Preparing of copper oxides thin films by chemical bath deposition (CBD) for using in environmental application. *Energy Procedia* **2015**, *74*, 1459–1465. [CrossRef]
41. Mallick, P.; Sahu, S. Structure, microstructure and optical absorption analysis of CuO nanoparticles synthesized by sol-gel route. *Nanosci. Nanotechnol.* **2012**, *2*, 71–74. [CrossRef]
42. Li, C.; Yin, Y.; Hou, H.; Fan, N.; Yuan, F.; Shi, Y.; Meng, Q. Preparation and characterization of Cu(OH)₂ and CuO nanowires by the coupling route of microemulsion with homogenous precipitation. *Solid. State Commun.* **2010**, *150*, 585–589. [CrossRef]
43. Saravanan, V.; Shankar, P.; Mani, G.K.; Bosco, J.; Rayappan, B. Growth and characterization of spray pyrolysis deposited copper oxide thin films: Influence of substrate and annealing temperatures. *J. Anal. Appl. Pyrol.* **2015**, *111*, 272–277. [CrossRef]
44. Wang, R.; Sui, Y.; Huang, S.; Pu, Y.; Cao, P. High-performance flexible all-solid-state asymmetric supercapacitors from nanostructured electrodes prepared by oxidation-assisted dealloying protocol. *Chem. Eng. J.* **2018**, *331*, 527–535. [CrossRef]
45. Singh, B.K.; Shaikh, A.; Dusane, R.O.; Parida, S. Copper oxide nanosheets and nanowires grown by one-step linear sweep voltammetry for supercapacitor application. *J. Energy Storage* **2020**, *31*, 101631. [CrossRef]
46. Toboonsung, B.; Singjai, P. Formation of CuO nanorods and their bundles by an electrochemical dissolution and deposition process. *J. Alloys Compd.* **2011**, *509*, 4132–4137. [CrossRef]
47. Wang, W.; Zhan, Y.; Wang, G. One-step, solid-state reaction to the synthesis of copper oxide nanorods in the presence of a suitable surfactant. *Chem. Commun.* **2001**, *8*, 727–728. [CrossRef]
48. Jiang, X.; Herricks, T.; Xia, Y. CuO nanowires can be synthesized by heating copper substrates in air. *Nano Lett.* **2002**, *2*, 1333–1338. [CrossRef]
49. Liu, J.; Xue, D. Thermal oxidation strategy towards porous metal oxide hollow architectures. *Adv. Mater.* **2008**, *20*, 2622–2627. [CrossRef]
50. Singh, D.P.; Ali, N. Synthesis of TiO₂ and CuO nanotubes and nanowires. *Sci. Adv. Mater.* **2010**, *2*, 295–335. [CrossRef]
51. Xu, C.H.; Woo, C.H.; Shi, S.Q. Formation of CuO nanowires on Cu foil. *Chem. Phys. Lett.* **2004**, *399*, 62–66. [CrossRef]
52. Liang, J.; Kishi, N.; Soga, T.; Jimbo, T. Cross-sectional characterization of cupric oxide nanowires grown by thermal oxidation of copper foils. *App Surf. Sci.* **2010**, *257*, 62–66. [CrossRef]
53. Goncalves, A.M.B.; Campos, L.C.; Ferlauto, A.S.; Lacerda, R.G. On the growth and electrical characterization of CuO nanowires by thermal oxidation. *J. Appl. Phys.* **2009**, *106*, 034303. [CrossRef]
54. Nkhaili, L.; Narjis, A.; Agdad, A.; Tchenka, A.; El Kissani, A.; Outzourhit, A.; Oueriagli, A. A simple method to control the growth of copper oxide nanowires for solar cells and catalytic applications. *Adv. Cond. Matter Phys.* **2020**, *2020*, 5470817. [CrossRef]
55. Castrejón-Sánchez, V.-H.; Solís, A.C.; López, R.; Encarnación-Gómez, C.; Morales, F.M.; Vargas, O.S.; Mastache-Mastache, J.E.; Sánchez, G.V. Thermal oxidation of copper over a broad temperature range: Towards the formation of cupric oxide (CuO). *Mater. Res. Express* **2019**, *6*, 075909. [CrossRef]
56. Holzwarth, U.; Gibson, N. The Scherrer Equation versus the ‘Debye-Scherrer Equation’. *Nat. Nanotechnol.* **2011**, *6*, 534. [CrossRef] [PubMed]
57. Kosicek, M.; Zavasnik, J.; Baranov, O.; Batic, S.B.; Cvelbar, U. Understanding the Growth of Copper Oxide Nanowires and Layers by Thermal Oxidation over a Broad Temperature Range at Atmospheric Pressure. *Cryst. Growth Des.* **2022**, *22*, 6656–6666. [CrossRef]
58. Lamberti, A.; Fontana, M.; Bianco, S.; Tresso, E. Flexible solid-state Cu_xO-based pseudo-supercapacitor by thermal oxidation of copper foils. *Int. J. Hydrogen Energy* **2016**, *41*, 11700–11708. [CrossRef]
59. Olabi, A.G.; Abbas, Q.; Abdelkareem, M.A.; Alami, A.H.; Mirzaeian, M.; Sayed, E.T. Carbon-Based Materials for Supercapacitors: Recent Progress, Challenges and Barriers. *Batteries* **2022**, *9*, 19. [CrossRef]
60. Schoetz, T.; Gordon, L.W.; Ivanov, S.; Bund, A.; Mandler, D.; Messinger, R.J. Disentangling faradaic, pseudocapacitive, and capacitive charge storage: A tutorial for the characterization of batteries, supercapacitors, and hybrid systems. *Electrochim. Acta* **2022**, *412*, 140072. [CrossRef]
61. Orgen, S.B.; Balela, M.D.L. Effect of Reaction Time on the Morphology of CuO Nanostructured Electrode for Pseudocapacitor Application. *J. Phys. Conf. Ser.* **2021**, *1974*, 012006. [CrossRef]
62. Sun, B.; Yao, M.; Chen, Y.; Tang, X.; Hu, W.; Pillai, S.C. Facile fabrication of flower-like γ-Fe₂O₃ @PPy from iron rust for high-performing asymmetric supercapacitors. *J. Alloy Compound.* **2022**, *922*, 166055. [CrossRef]
63. Sun, J.; Guo, L.; Sun, X.; Zhang, J.; Hou, L.; Li, L.; Yang, S.; Yuan, C. One-Dimensional Nanostructured Pseudocapacitive Materials: Design, Synthesis and Applications in Supercapacitors. *Batter. Supercaps* **2019**, *2*, 820–841. [CrossRef]
64. Gund, G.S.; Dubal, D.P.; Chodankar, N.R.; Cho, J.Y.; Gomez-Romero, P.; Park, C.; Lokhande, C.D. Low-cost flexible supercapacitors with high-energy density based on nanostructured MnO₂ and Fe₂O₃ thin films directly fabricated onto stainless steel. *Sci. Rep.* **2015**, *5*, 12454. [CrossRef] [PubMed]
65. Permatasari, F.A.; Irham, M.A.; Bisri, S.Z.; Iskandar, F. Carbon-Based Quantum Dots for Supercapacitors: Recent Advances and Future Challenges. *Nanomaterials* **2021**, *11*, 91. [CrossRef] [PubMed]

66. Sayyed, S.G.; Shaikh, A.V.; Shinde, U.P.; Hiremath, P.; Naik, N. Copper oxide-based high-performance symmetric flexible supercapacitor: Potentiodynamic deposition. *J. Mater. Sci. Mater. Electron.* **2023**, *34*, 1361. [[CrossRef](#)]
67. Shinde, S.K.; Dubal, D.P.; Ghodake, G.S.; Gomez-Romero, P.; Kim, S.; Fulari, V.J. Influence of Mn incorporation on the supercapacitive properties of hybrid CuO/Cu(OH)₂ electrodes. *RSC Adv.* **2015**, *5*, 30478–30484. [[CrossRef](#)]
68. Dey, R.S.; Hjuler, H.A.; Chi, Q. Approaching the theoretical capacitance of graphene through copper foam integrated three-dimensional graphene networks. *J. Mater. Chem. A* **2015**, *3*, 6324–6329. [[CrossRef](#)]
69. Wang, L.; Hu, J.; Jiang, L.; Li, X.; Cao, J.; Wang, Q.; Wang, A.; Li, X.; Qu, L.; Lu, Y. High-performance 3D CuO/Cu flowers supercapacitor electrodes by femtosecond laser enhanced electrochemical anodization. *Electrochim. Acta* **2019**, *293*, 273–282. [[CrossRef](#)]
70. He, D.; Wang, G.; Liu, G.; Suo, H.; Zhao, C. Construction of Leaf-Like CuO-Cu₂O Nanocomposite on Copper Foam for High-Performance Supercapacitors. *Dalton Trans.* **2017**, *46*, 3318–3324. [[CrossRef](#)] [[PubMed](#)]
71. Zhang, W.; Lau, K.S.; Chia, C.H.; Umar, A.A.; Mohamed, M.A.; Buyong, M.R.; Hamzah, A.A. Fabrication and Characterization of Supercapacitor Electrode with Amorphous CuO/Crystalline Cu₂O/Porous Cu Composite Based on Copper Foil Substrate. 2023; book chapter. [[CrossRef](#)]
72. Sepahvand, S.; Ghasemi, S.; Sanaee, Z. Electric Field Enhanced Synthesis of Copper Hydroxide Nanostructures for Supercapacitor Application. *NANO Brief Rep. Rev.* **2017**, *12*, 1750010. [[CrossRef](#)]
73. Yin, Z.; Wang, X.; Song, M.; Wu, Z.; Li, Z.; Wang, X.; Zhu, M.; Liu, D.; Zhao, J. Facile fabrication of Cu₂O/Cu columnar array electrode through dealloying and in situ oxidation for supercapacitor applications. *J. Solid State Electrochem.* **2020**, *24*, 1313–1324. [[CrossRef](#)]
74. Yao, P.; Li, C.; Yu, J.; Zhang, S.; Zhang, M.; Liu, H.; Ji, M.; Cong, G.; Zhang, T.; Zhu, C. High performance flexible energy storage device based on copper foam supported NiMoO₄ nanosheets-CNTs-CuO nanowires composites with core–shell holey nanostructure. *J. Mater. Sci. Technol.* **2021**, *85*, 87–94. [[CrossRef](#)]
75. Patil, A.S.; Patil, M.D.; Lohar, G.M.; Jadhav, S.T.; Fulari, V.J. Supercapacitive properties of CuO thin films using modified SILAR method. *Ionics* **2016**, *23*, 1259–1266. [[CrossRef](#)]
76. Pawar, S.M.; Kim, J.; Inamdar, A.I.; Woo, H.; Jo, Y.; Pawar, B.S.; Cho, S.; Kim, H.; Im, H. Multi-functional reactively-sputtered copper oxide electrodes for supercapacitor and electro-catalyst in direct methanol fuel cell applications. *Sci. Rep.* **2016**, *6*, 21310. [[CrossRef](#)] [[PubMed](#)]

Disclaimer/Publisher’s Note: The statements, opinions and data contained in all publications are solely those of the individual author(s) and contributor(s) and not of MDPI and/or the editor(s). MDPI and/or the editor(s) disclaim responsibility for any injury to people or property resulting from any ideas, methods, instructions or products referred to in the content.